Propylamine hydrobromide passivated tin-based perovskites to efficient solar cells

Xiaomeng Li, Pengcheng Jia, Fanwen Meng, Xingyu Zhang, Yang Tang, Bo Song, Chang Gao, Liang Qin, Feng Teng, and Yanbing Hou

View the article online at SpringerLink or IJMMM Webpage.

Articles you may be interested in

Huan-yu Zhang, Rui Li, Wen-wu Liu, Mei Zhang, and Min Guo, Research progress in lead-less or lead-free three-dimensional perovskite absorber materials for solar cells, *Int. J. Miner. Metall. Mater.*, 26(2019), No. 4, pp. 387-403. https://doi.org/10.1007/s12613-019-1748-2

Jing-cheng Wang, Lei Li, and Yong Yu, Tin recovery from a low-grade tin middling with high Si content and low Fe content by reduction–sulfurization roasting with anthracite coal, *Int. J. Miner. Metall. Mater.*, 28(2021), No. 2, pp. 210-220. https://doi.org/10.1007/s12613-020-2038-8

Mohamed Reda Boudchicha, Fausto Rubio, and Slimane Achour, Synthesis of glass ceramics from kaolin and dolomite mixture, *Int. J. Miner. Metall. Mater.*, 24(2017), No. 2, pp. 194-201. https://doi.org/10.1007/s12613-017-1395-4

Xiao-hui Ning, Chen-zheng Liao, and Guo-qing Li, Electrochemical properties of Ca–Pb electrode for calcium-based liquid metal batteries, *Int. J. Miner. Metall. Mater.*, 27(2020), No. 12, pp. 1723-1729. https://doi.org/10.1007/s12613-020-2150-9

Chun-bao Sun, Xiao-liang Zhang, Jue Kou, and Yi Xing, A review of gold extraction using noncyanide lixiviants: Fundamentals, advancements, and challenges toward alkaline sulfur-containing leaching agents, *Int. J. Miner. Metall. Mater.*, 27(2020), No. 4, pp. 417-431. https://doi.org/10.1007/s12613-019-1955-x

Hong-pan Liu, Xiao-feng Huang, Li-ping Ma, Dan-li Chen, Zhi-biao Shang, and Ming Jiang, Effect of Fe_2O_3 on the crystallization behavior of glass-ceramics produced from naturally cooled yellow phosphorus furnace slag, *Int. J. Miner. Metall. Mater.*, 24(2017), No. 3, pp. 316-323. https://doi.org/10.1007/s12613-017-1410-9

IJMMM WeChat   QQ author group

Propylamine hydrobromide passivated tin-based perovskites to efficient solar cells

Xiaomeng Li, Pengcheng Jia, Fanwen Meng, Xingyu Zhang, Yang Tang, Bo Song, Chang Gao, Liang Qin✉, *Feng Teng, and Yanbing Hou*✉

Key Laboratory of Luminescence and Optical Information, Beijing Jiaotong University, Beijing 100044, China

Abstract: The development of tin-based devices with low toxicity is critical for the commercial viability of perovskite solar cells. However, because tin halide is a stronger Lewis acid, its crystallization rate is extremely fast, resulting in the formation of numerous defects that affect the device performance of tin-based perovskite solar cells. Herein, propylamine hydrobromide (PABr) was added to the perovskite precursor solution as an additive to passivate defects and fabricate more uniform and dense perovskite films. Because propylamine cations are too large to enter the perovskite lattices, they only exist at the grain boundary to passivate surface defects and promote crystal growth in a preferred orientation. The PABr additive raises the average short-circuit current density from 19.45 to 25.47 mA·cm^{-2} by reducing carrier recombination induced by defects. Furthermore, the device's long-term illumination stability is improved after optimization, and the hysteresis effect is negligible. The addition of PABr results in a power conversion efficiency of 9.35%.

Keywords: tin-based perovskite solar cells; propylamine hydrobromide; passivation; crystallization

1. Introduction

Due to their high conversion efficiency, simple fabrication process, and low cost of production, perovskite solar cells (PSCs) have emerged as one of the most promising third-generation of solar cells [1]. The power conversion efficiency (PCE) of lead-based PSCs has increased from 3.8% to 25.7% in the last decade. However, because lead toxicity has significantly hampered commercial interest in lead-based PSCs, less-toxic tin-based perovskites have been proposed as the most promising substitutes for lead perovskites [2–9]. Three major limitations of tin-based PSCs, however, must be addressed. First, tin-based perovskite materials exhibit a low vacancy formation energy [10–15]. Sn^{2+} oxidizes easily to Sn^{4+}, resulting in severe p-type self-doping of Sn-based perovskite films. Furthermore, when compared to lead, the energy levels of tin-based perovskites are mismatched with those of carrier transport materials, resulting in a significant loss of open-circuit voltage (V_{OC}) [16–17]. Finally, due to the high crystallization rate of tin-based perovskite, solution processing is difficult to achieve uniform and dense films [14,18–20]. Inferior morphology would result in severe carrier recombination induced by defects, affecting carrier transport and extraction efficiency [21–23].

One of the most efficient methods for producing high-quality tin-based perovskite films is to use appropriate passivators [24–27]. The device's open-circuit voltage can be increased by inserting larger organic cations to establish a quasi-two-dimensional structure or by doping X-halogen to modify the energy band gap [28–30]. However, because doping at the X-site anion would cause phase separation of tin-based perovskites under long-term illumination, A-site cation doping is a popular research area [31–33]. To alleviate surface trap states and increase the V_{OC} of tin-based PSCs, adequate passivators such as Lewis base molecules, polymers, or 2-dimensional (2D) phases perovskite with wide band gaps have been developed [34–37]. To reduce the surface defect density of perovskite films, Lewis base molecules, such as organic amine, choline, and thiol, have frequently been used as passivators [38–41]. Jokar *et al.* [42] were the first to use ethylene diammonium diiodide (EDAI$_2$) to passivate tin perovskite films. The researchers discovered that EDAI$_2$ has a slow passivation effect on surface defects, which increases the carrier lifetime of a tin perovskite film. Because of the creation of Lewis adducts between uncoordinated Sn atoms and the dimethylamino of [tetraphenylethene 3,3'-(((2,2-diphenylethene-1,1-diyl) bis(4,1-phenylene)) bis(oxy)) bis (N,N-dimethylpropan-1-amine) tetraphenylethene] (PTN-Br), the passivation of trap states in perovskite layer by conjugated polymer PTN-Br was reported by Liu *et al.* [43]. Jokar *et al.* [44] reported a sequential deposition procedure that improved the photoluminescence lifetime and charge-extraction rate of a mixed cationic tin perovskite solar cell by passivating the surface with a trifluoroethanol solution of

✉ Corresponding authors: Liang Qin   E-mail: qinliang@bjtu.edu.cn;   Yanbing Hou   E-mail: ybhou@bjtu.edu.cn

phenylhydrazinium thiocyanate (PHSCN). By controlling the A-site cation, Nishimura *et al.* [45] achieved high-efficiency tin-based solar cells with a tolerance factor of about 1. Proper passivation can also improve device stability [46]. By adding hydroxybenzene sulphonic acid or its salt to the perovskite precursor solution, air-stable FASnI$_3$ solar cells were accomplished. Furthermore, antioxidant passivation significantly improves the oxidation stability of tin-based PSCs [47].

Propylamine hydrobromide (PABr) was added to the perovskite precursor solution as an additive to reduce defect-induced carrier recombination in this work. Propylamine cations (PA$^+$) with long chains cannot enter the perovskite lattice but exist at the grain boundary, passivating perovskite grain surface defects and promoting crystal formation in a preferred orientation. Doping the perovskite precursor solution with 0.02 M PABr improves device performance significantly. The short-circuit current density (J_{SC}) of devices with PABr increases significantly. As a result, the PCE of the device developed from the PABr-added precursor solution achieved a conversion efficiency of 9.35%, which is more than 38% higher than the PCE of the control device.

2. Experimental

2.1. Materials

Heraeus Clevios supplied the poly(3,4-ethylenedioxythiophene):poly(styrene sulfonate) (PEDOT:PSS, Clevious PVP Al 4083). Xi'an Polymer Light Technology provided formamidinium iodide (FAI), propylamine hydrobromide (PABr), and Bathocuproine (BCP). 99.999% ultra-dry tin(II) iodide (SnI$_2$) was purchased from Alfa Aesar. Sigma-Aldrich supplied tin(II) fluoride (SnF$_2$), N,N-dimeth-ylformamide (DMF) of 99.8%, dimethyl sulfoxide (DMSO) of 99.8%, and hydrazine monohydrobromide (N$_2$H$_5$Br). Buckminsterfullerene (C$_{60}$) was purchased from Nichem (Taiwan). All materials did not require any purification before use.

2.2. Perovskite precursor solution preparation

FAI (172 mg), SnI$_2$ (373 mg), SnF$_2$ (15.7 mg), and N$_2$H$_5$Br (4.5 mg) were dissolved in a mixture of DMF (928 μL) and DMSO (72 μL) to prepare a 1 mL FASnI$_3$ precursor solution. PABr (2.8 mg) was also dissolved in the PABr-doped perovskite precursor solution. All perovskite precursor solutions were magnetically agitated in a glove box for 12 h at 50°C.

2.3. Perovskite solar cell fabrication

The indium tin oxide (ITO) glass substrate was cleaned with a specific cleaning agent and immersed in deionized water for 30 min. The ultrasound is then repeated twice with anhydrous alcohol. The scrubbed ITO glass substrates were then treated for 120 s with plasma ozone. After shaking for 12 h and filtering through a 0.22 μm filter, the PEDOT:PSS solution was spin-coated on ITO substrates for 40 s at 4000 r/min and then annealed at 150°C for 15 min. Dry PEDOT:PSS-coated substrates were placed in a glove box. The perovskite precursor solution was spin-coated on the PEDOT:PSS at 5000 r/min for 20 s and then the solution was

filtered with a 0.22 μm filter. As an antisolvent, 80 mL of toluene was used to treat the perovskite films during the spin coating procedure. FASnI$_3$ perovskite films were annealed in the dark at 100°C for 10 min. C$_{60}$ (40 nm) and BCP (6 nm) were then deposited using vacuum evaporation in a vacuum chamber with a vacuum degree less than 4×10^{-4} Pa. Finally, under the same vacuum conditions, Ag (90 nm) was deposited on the BCP layer to fabricate an electrode with a surface area of 0.045 cm^2.

2.4. Film and device characterization

A field emission scanning electron microscope was used to capture scanning electron microscopy (SEM) images (ZEISS G300, 15 kV). The X-ray diffraction (XRD) patterns of the perovskite films were captured using a Bruker D8 X-ray diffractometer and Cu K radiation (40 kV, 40 mA). A Shimadzu UV-3101PC spectrophotometer was used to measure absorbance. Photoluminescence (PL) spectroscopy was evaluated using a HORIBA iHR 320. TCSPC (time-correlated single photon counting) measurements were used to quantify time-resolved photoluminescence (TRPL) (Fluoro-Cube-01-NL). A Keithley 2450 Source Measure Unit was used to measure the current density–voltage (*J–V*) characteristics of PSCs. The device's performance was monitored continuously on a solar simulator (Zolix Sirius-SS150A-D solar simulator) under AM 1.5 G illumination of 100 mW·cm^{-2}. A total of 101 test points was scanned across a voltage range of −0.2 to 0.8 V. The Zolix Solar Cell Scan 100 was used to calculate the external quantum efficiency (EQE). The residual charges and transient photovoltage were measured using a digital oscilloscope (Tektronix MSO5104B) with an open-circuit state input impedance of 1 MΩ. An arbitrary function generator powered the pulse light source, a concentrated cool white LED. Transient current (TPC) and transient photovoltage (TPV) were measured using a digital oscilloscope while exposed to a Nd^{3+}:YAG laser. For TPC and TPV measurements, the oscilloscope's input impedance was set to 50 Ω and 1 MΩ, respectively. Meanwhile, TPC and TPV were measured with 1 Sun background illumination and a minor perturbation of approximately 5% amplitude caused by the excitation of a Nd^{3+}:YAG laser pulse.

3. Results and discussion

The crystallization quality and morphology of the perovskite active layer strongly influence the performance of tin-based perovskite devices. Using SEM, we first investigated the effect of PABr as an additive on the morphology of FASnI$_3$ perovskite films. The film without PABr is referred to as the control perovskite film, whereas the film with PABr is referred to as the PABr perovskite film. Fig. 1 shows top-view and sectional SEM images of the control perovskite film and PABr perovskite film. Compared to the control perovskite film, the grain size of the PABr perovskite film increases while the grain boundaries decrease. According to the grain size distribution of the perovskite films, the average perovskite grain size increased from 248 to 371 nm (Fig. S1). One grain of PABr perovskite film can penetrate the entire
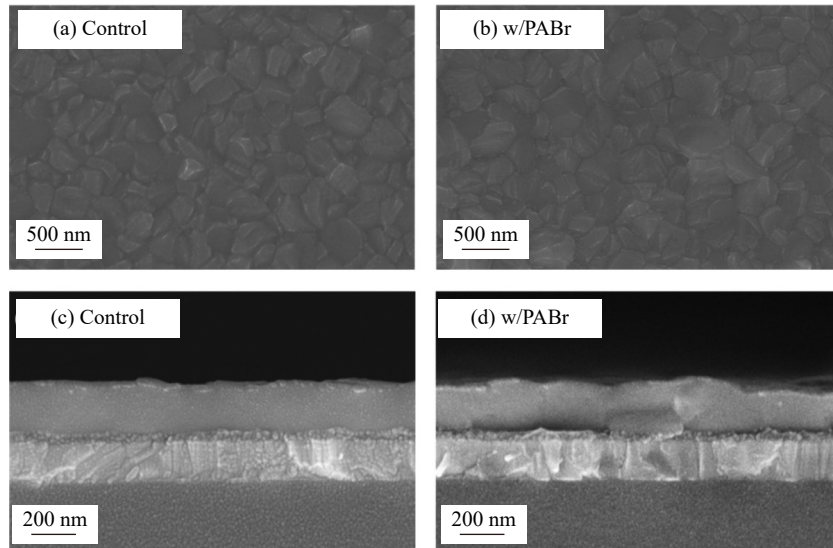
Fig. 1. Top-view SEM images of perovskite films (a) without and (b) with PABr (w/PABr). Sectional view SEM images of (c) control perovskite film and (d) PABr perovskite film.

absorbent layer perpendicular to the substrate, and the grains in the PABr perovskite film have clearer grain boundaries than the grains in the control perovskite film. Normally, defects at the grain boundary would act as the traps for carriers, resulting in defect-induced carrier recombination and lowering the carrier extraction ability and carrier lifetime of perovskite films. PABr can successfully passivate defects at perovskite grain boundaries and increase grain size, thereby improving perovskite active layer crystallization quality.

Fig. 2(a) shows a schematic diagram of the crystal structure of FASnI$_3$ perovskite doped with PABr. An appropriate empirical Goldschmidt tolerance factor is required to stabilize the 3-dimensional (3D) perovskite structure. Goldschmidt's tolerance factor (t_f) formula states:

$$t_f = \frac{R_A + R_B}{\sqrt{2}(R_B + R_X)} \tag{1}$$

where R_A and R_B denote the radii of A-site and B-site cations,
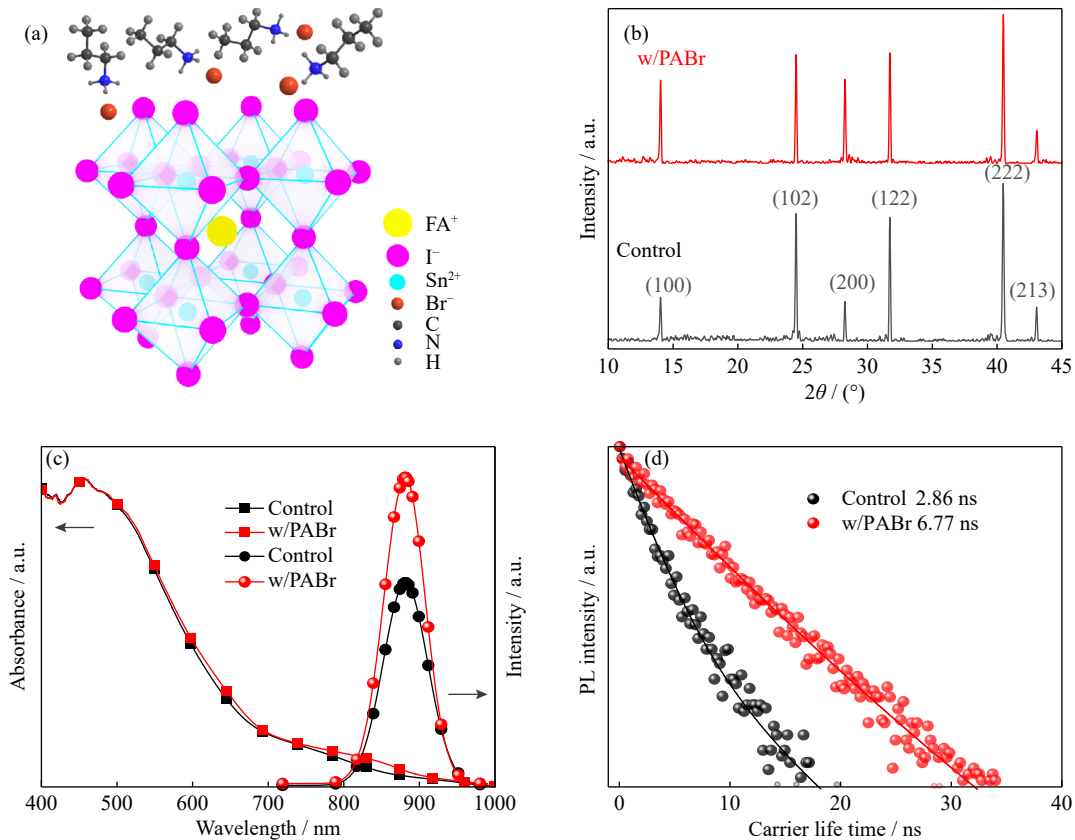

Fig. 2. (a) Schematic diagram of the crystal structure of FASnI$_3$ perovskite doped with PABr. (b) XRD patterns of perovskite films without and with PABr. (c) Absorption and PL spectra of control perovskite film and PABr perovskite films. (d) TRPL of FASnI$_3$ films without and with PABr additive.

respectively, and R_X is the anion radius. The cubic crystal structure is stable if the tolerance factor is between 0.813 and 1.107 [48]. According to the empirical formula of tolerance factor forming the 3D perovskite stable structure, the size of PA^+ is too large to enter the perovskite lattice, so PA^+ is spread beyond the usual octahedral arrangement of perovskite [49–50]. The XRD patterns of perovskite films without and with PABr are shown in Fig. 2(b). The characteristic crystal planes (100), (102), (200), (122), (222), and (213) are assigned to six FASnI$_3$ phase diffraction peaks at approximately 14.04°, 24.49°, 28.25°, 31.66°, 40.38°, and 42.97° in the XRD pattern. The XRD dominant peak intensity of the PABr perovskite film is significantly increased, particularly for promoting crystal growth toward preferred crystal orientations of (100) and (200), indicating that the addition of PA^+ does not change the crystal structure of the orthogonal perovskite but affords orderly perovskite grain distribution. Table S1 shows the XRD peak intensity ratios of the (100) crystal facet to other crystal facets for perovskite films with and without PABr. The results show that for the PABr perovskite films, the relative peak intensity of the (100) crystal planes increase, proving that PABr can facilitate growth in the (100) direction. After adding PABr, the overall full width at half maxima (FWHM) of the XRD peaks narrowed, with the FWHM of the (100) peak decreasing to 0.127° from 0.131°. Meanwhile, when PABr is introduced, small angular shifts are recorded (as depicted in Fig. S2 and Table S2).

The optical properties of the prepared films were evaluated in addition to their structure and morphology. Fig. 2(c) depicts the absorption and PL spectra of perovskite films. The absorption of the perovskite film is unaffected by wheth-

er PABr is doped. The changes in the steady-state PL spectra are easily determined. The PL peaks of the two types of perovskite films are located around 880 nm, and the PL emission of the PABr perovskite film is more intense than that of the control one, indicating that defect-induced recombination of carriers in the perovskite with PABr is significantly suppressed. Furthermore, the TRPL curves of perovskite films were measured using a 532 nm pulse laser, as shown in Fig. 2(d). The lifetime of an excited state is calculated using the following formula based on the TRPL curve:

$$Y = A + B_1 e^{(-t/\tau_1)} + B_2 e^{(-t/\tau_2)} \tag{2}$$

The TRPL decay time constants (τ_1 and τ_2) correspond to the lifetimes of excited states inside and on the surface of the grains, respectively (B_1 and B_2 are relative amplitudes). The accurate parameters of carrier lifetime are shown in Table S3. τ_1 is 2.27 ns with an 84.27% ratio for the control perovskite film, and τ_2 is 6.70 ns with a 12.78% ratio. τ_1 is 6.06 ns with a 70.44% ratio for the PABr perovskite film, and τ_2 is 9.72 ns with a 16.93% ratio. The excited state lifetimes (τ_{avg}) in the control perovskite film and the PABr perovskite film are 2.86 and 6.77 ns, respectively. The improvement in perovskite crystallization quality and PA^+ passivation reduces defects inside and on the surface of the perovskite film, slowing carrier recombination induced by the defects. The long lifetime of the excited state is critical in improving the PSCs open-circuit voltage (V_{OC}) and short-circuit current.

We used a p-i-n structure device to fabricate planar PSCs. Fig. 3(a) depicts the structure of the FASnI$_3$ perovskite device, while Fig. 3(b) depicts the energy-level diagram of the related material [51]. The device without the additive is labeled as a control device, while the device with PABr as an
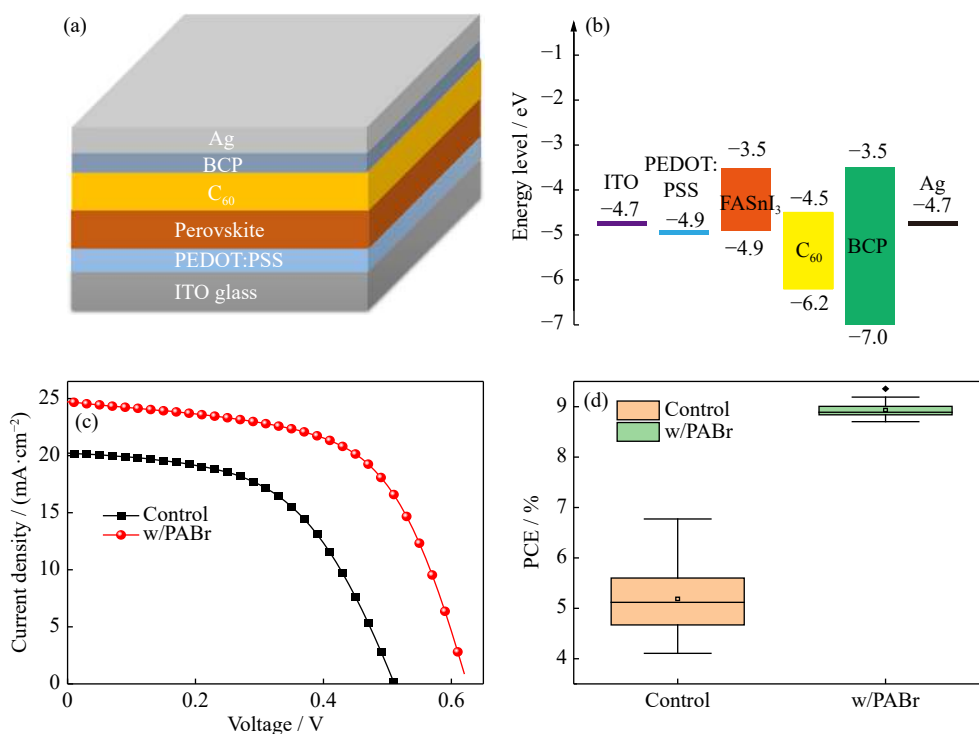

Fig. 3. (a) Structure of FASnI$_3$ perovskite devices. (b) Energy-level diagram of related materials. (c) *J–V* curves of the control and PABr champion devices under forward scan. (d) PCE box diagram of the control and PABr devices.

additive is labeled as a PABr device. The devices' J–V curves are shown in Fig. 3(c). The addition of PABr was discovered to significantly improve device performance. PABr devices perform admirably, with a champion PCE of 9.35%, a V_{OC} of 0.63 V, a J_{SC} of 26.79 mA/cm², and a fill factor (FF) of 63.70%. Fifty control and PABr devices were fabricated and tested, and the PCE box diagram of the device is shown in Fig. 3(d), indicating that the addition of PABr improved the efficiency of the PSCs significantly. Table 1 summarizes the photovoltaic parameters of the devices.

Fig. 4(a) depicts the PL spectra of perovskite films with varying PABr molar ratios. The PL intensity rises and reaches its maximum at 0.02 M PABr addition, then declines with increasing PABr concentration, which is consistent with the device's performance with 0.02 M PABr, as shown in

Fig. 4(b). Furthermore, the J–V curves of the PABr device measured in forward and reverse scanning (Fig. 4(c)) are nearly identical, indicating that the PABr device's J–V hysteresis is negligible, which may be related to the reduction of surface defects due to PA$^+$ passivation. The hysteresis of the J–V curve would result from ionic migration along grain boundaries. The J–V hysteresis curves of the control devices show an obvious hysteresis effect compared to the PABr device, demonstrating that PABr passivation can reduce grain boundaries and inhibit the device's hysteresis effect. The PABr device's maximum steady-state PCE was also measured at a bias of 0.47 V under AM 1.5 G illumination of 100 mW·cm^{-2}. After 400 s of irradiation, the PCE dropped to about 7.8% (Fig. S3).

Table 1.   Photovoltaic parameters of the control and PABr devices

FASnI$_3$ perovskite	V_{OC} / V		J_{SC} / (mA·cm^{-2})		PCE / %		FF / %	
	Champion	Average	Champion	Average	Champion	Average	Champion	Average
Control	0.55	0.51 ± 0.01	22.52	19.45 ± 1.30	6.77	5.19 ± 0.68	54.08	52.14 ± 3.08
w/PABr	0.63	0.60 ± 0.02	26.79	25.47 ± 0.69	9.35	8.93 ± 0.16	63.70	60.04 ± 1.67

Note: The measurement was performed with 100 mW/cm² of AM 1.5 G illumination, simulating solar illumination. Fifty devices were used to calculate the average value.
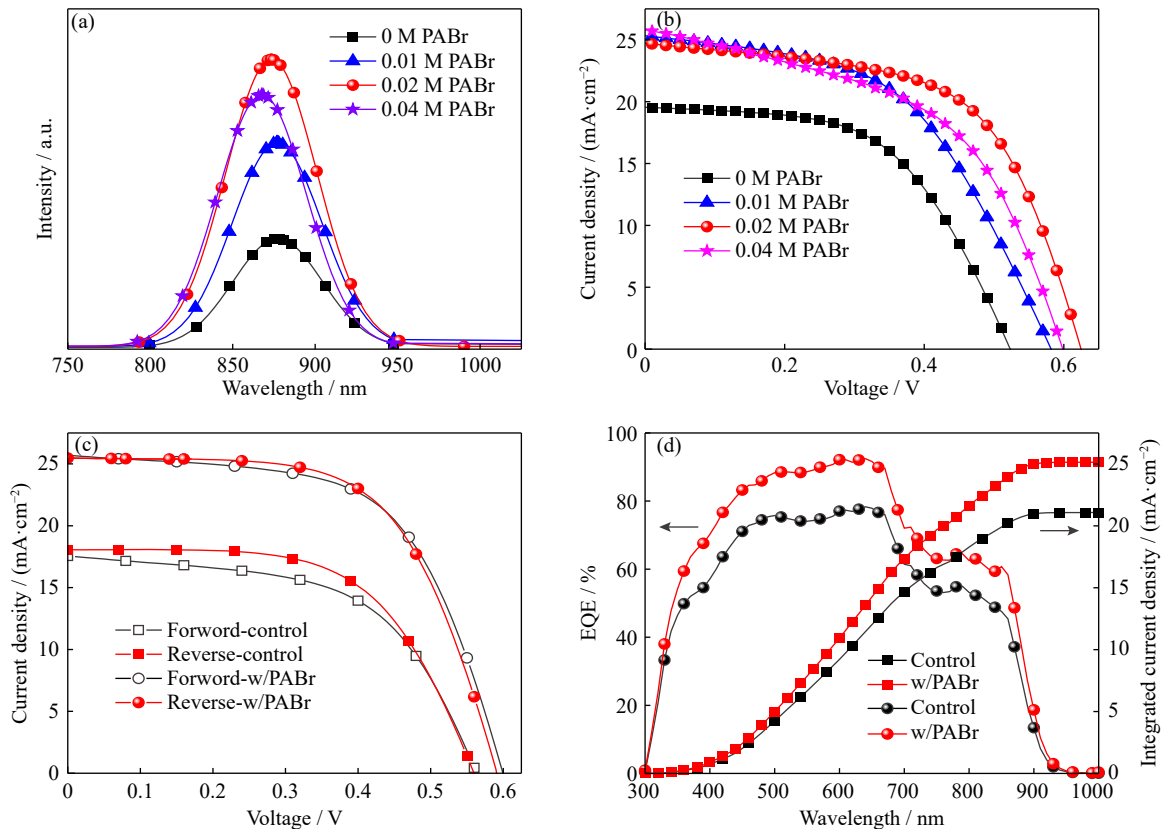

Fig. 4.   (a) PL spectra and (b) J–V curves of devices based on FASnI$_3$ with different proportions of PABr. (c) J–V hysteresis curves of the control device and PABr device. (d) EQE spectra and integrated J_{SC}.

Furthermore, as shown in Fig. 4(d), the integral current densities obtained from the EQE curve are 25.14 mA·cm^{-2} for the PABr device and 21.08 mA/cm² for the control device. The result of PABr device is less than that of the J–V curves. The device's performance loss in the two test opera-

tions could be attributed to oxidation. Meanwhile, the V_{OC} and J_{SC} short-term light stability of the PABr device and control device were measured and shown in Figs. S4 and S5. Both V_{OC} and J_{SC} decrease once the illumination is turned on, then stabilize after 100 s, which is consistent with PCE short-

term stability. The test results of the 480-h stability of the control and PABr devices in the N_2 glove box are shown in Fig. S6. The PCE of the control devices fell to 56% of their initial value, while the PCE of PABr devices remained at 76%, demonstrating the enhanced stability of PABr devices.

The dependence of V_{OC} on light intensity was also measured to better understand the mechanisms of defect-assisted recombination. Using the following equation, the ideality factor n can be calculated from the dependence of V_{OC} on the light intensity (I) curve:

$$\frac{\mathrm{d}V_{oc}}{\mathrm{d}(\ln I)} = \frac{nkT}{q} \tag{3}$$

where k denotes the Boltzmann constant, T denotes the temperature in K, and q denotes the elementary charge. Generally, the n of photovoltaic devices is between 1 and 2, where $n = 2$ suggests that trap-assisted recombination predominates and $n = 1$ implies that carrier–carrier recombination predominates [25]. The n values of the control device and the PABr device are 1.61 and 1.29, respectively, as shown in Fig. 5(a), indicating that the density of defects in the device with the addition of PABr is less than that of the control device. The residual charge test was also used to characterize deep-level defects in the two devices, as shown in Fig. 5(b). When the electromagnetic relay in the circuit is turned on, these devices are short-circuited [52]. After that, the photogenerated charges would be discharged and neutralized, and V_{OC} would be zero. On the other hand, the V_{OC} of PSCs rises initially when the electromagnetic relay is turned off due to the re-

lease and redistribution of trapped charges by deep-level defects. The amount of V_{OC} rebound can be related to the number of trapped carriers. The control device's V_{OC} rebound is much greater than that of the PABr device, indicating that there are more trapped carriers in the control device. More trapped carriers imply more deep-level defects. The reduction in trapped carriers demonstrates that the density of deep-level defects in the PABr device has been effectively reduced. The defect density was further evaluated using the space charge limited current method, as shown in Fig. S7. The hole-only devices were fabricated using the ITO/PEDOT:PSS/perovskite/MoO$_3$/Ag architecture, and the defect density was calculated using the following equation:

$$N_t = \frac{2\varepsilon\varepsilon_0 V_{TFL}}{qL^2} \tag{4}$$

where N_t denotes the hole trap density, ε denotes the dielectric constant of perovskite, ε_0 denotes the dielectric constant of vacuum, V_{TFL} denotes the voltage at which all the traps are filled, q denotes the elementary charge, and L denotes the thickness of the perovskite film. Adding PABr to the perovskite reduces the trap density from 1.58×10^{15} to 1.38×10^{15} cm^{-3}, demonstrating that PABr could passivate the defect trap state [53]. Furthermore, as shown in Fig. 5(c), the TPV test results of the control and PABr devices confirm that PABr addition can reduce the density of defects. The control and PABr devices have carrier lifetimes of 2.71 and 4.12 μs, respectively. The longer the carrier lifetime, the fewer the defects. Meanwhile, dark transient photovoltage tests in solar
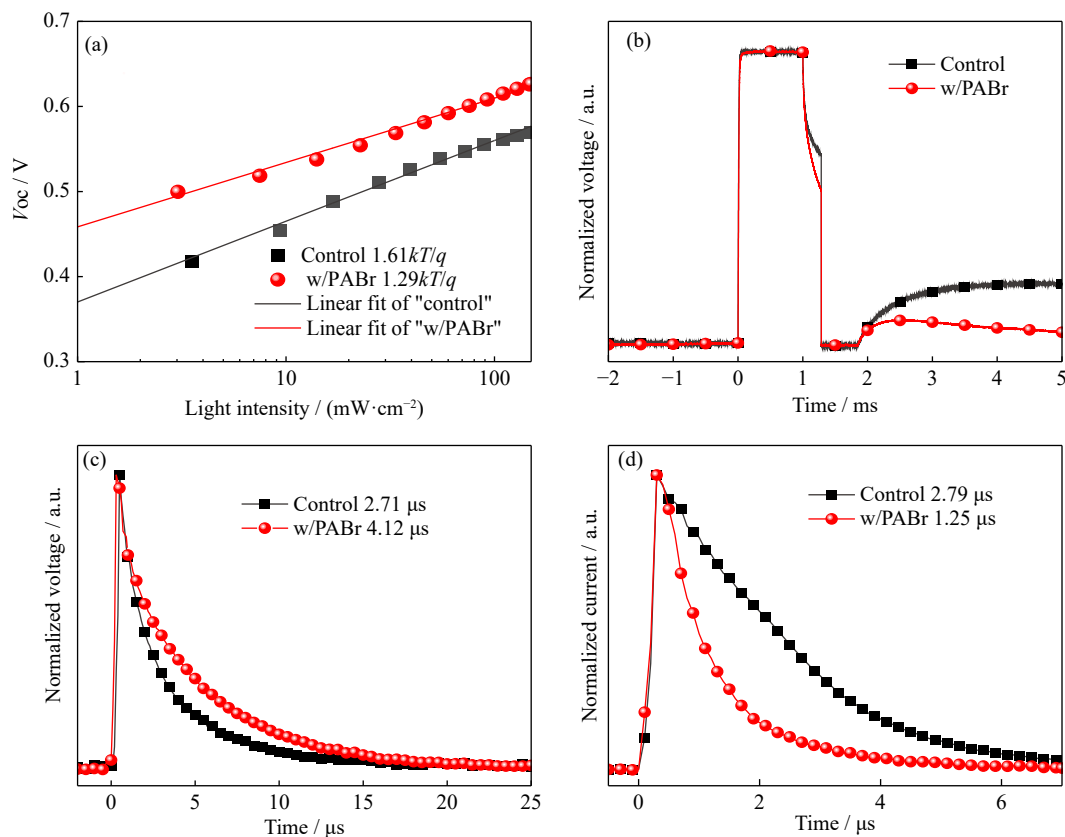

Fig. 5. (a) Light intensity-dependent V_{OC} curve and (b) residual charge test curve of the control device and PABr device. (c) TPV and (d) TPC response.

cells can characterize carrier recombination dynamics via defects and carrier de-trapping. As illustrated in Fig. S8, the decay time of the open-circuit voltage of the PABr device becomes significantly faster than that of the control device, demonstrating that the incorporation of PABr can effectively reduce the defect density in the perovskite layer. As shown in Fig. 5(d), the TPC test can confirm the effect of PABr addition on carrier extraction in the device. The photocurrent decay times of the control and PABr devices are 2.79 and 1.25 µs, respectively. The photocurrent decay time of the devices with PABr is significantly shorter than that of the control device, demonstrating that the addition of PABr can improve charge extraction efficiency due to perovskite grain orientation growth. The TPV and TPC measurements show that PABr can increase carrier lifetime and improve charge-extraction efficiency, resulting in improved device performance.

4. Conclusion

In summary, we have developed an efficient method for fabricating high-quality tin-based perovskite thin films in which PABr is used to passivate defects on the surface of perovskite grains. PABr not only passivates surface defects but also improves the crystal quality of FASnI$_3$ perovskite films. Furthermore, PABr could specifically induce crystal orientation growth in the direction of (100), which is conducive to forming good contact between the perovskite active layer and the hole transport layer. A solar cell based on the PABr-doped FASnI$_3$ exhibited improved device performance due to the reduction of surface defects, improvement in crystallinity, and orderly orientation. The PCE of the PABr-doped FASnI$_3$ solar cell is 9.35%, which is 38% higher than that of the control device. This study demonstrates that PA cations can passivate defects in tin-based perovskites and improve the performance of tin-based PSCs.

Acknowledgements

Conflict of Interest

The authors disclose no relevant relationship.

Supplementary Information

The online version contains supplementary material available at https://doi.org/10.1007/s12613-023-2604-y.

References

[1] M.A. Green, Y.J. Jiang, A.M. Soufiani, and A. Ho-Baillie, Optical properties of photovoltaic organic–inorganic lead halide perovskites, *J. Phys. Chem. Lett.*, 6(2015), No. 23, p. 4774.

[2] G.E. Eperon, S.D. Stranks, C. Menelaou, M.B. Johnston, L.M. Herz, and H.J. Snaith, Formamidinium lead trihalide: A broadly tunable perovskite for efficient planar heterojunction solar cells, *Energy Environ. Sci.*, 7(2014), No. 3, p. 982.

[3] S.R. Wang, X. Zhang, W.K. Zhu, *et al*., Lewis base manipulated crystallization for efficient tin halide perovskite solar cells, *Appl. Surf. Sci.*, 602(2022), art. No. 154393.

[4] P. You, G.J. Li, G.Q. Tang, J.P. Cao, and F. Yan, Ultrafast laser-annealing of perovskite films for efficient perovskite solar cells, *Energy Environ. Sci.*, 13(2020), No. 4, p. 1187.

[5] M.A. Green, A. Ho-Baillie, and H.J. Snaith, The emergence of perovskite solar cells, *Nat. Photonics*, 8(2014), No. 7, p. 506.

[6] M. Pitaro, E.K. Tekelenburg, S.Y. Shao, and M.A. Loi, Tin halide perovskites: From fundamental properties to solar cells, *Adv. Mater.*, 34(2022), No. 1, art. No. 2105844.

[7] S. Gu, R.X. Lin, Q.L. Han, Y. Gao, H.R. Tan, and J. Zhu, Tin and mixed lead–tin halide perovskite solar cells: Progress and their application in tandem solar cells, *Adv. Mater.*, 32(2020), No. 27, art. No. 1907392.

[8] National Renewable Energy Laboratory (NREL), *Best Research-Cell Efficiency Chart* [2022-08 -18]. https://www.nrel.gov/pv/cell-efficiency.html?tdsourcetag=s_pcqq_aiomsg.

[9] Z.B. Que, L. Chu, S.B. Zhai, *et al*., Self-assembled TiO$_2$ hole-blocking layers for efficient perovskite solar cells, *Int. J. Miner. Metall. Mater.*, 29(2022), No. 6, p. 1280.

[10] J.P. Cao and F. Yan, Recent progress in tin-based perovskite solar cells, *Energy Environ. Sci.*, 14(2021), No. 3, p. 1286.

[11] C.C. Boyd, R. Cheacharoen, T. Leijtens, and M.D. McGehee, Understanding degradation mechanisms and improving stability of perovskite photovoltaics, *Chem. Rev.*, 119(2019), No. 5, p. 3418.

[12] R.L. Milot, M.T. Klug, C.L. Davies, *et al*., The effects of doping density and temperature on the optoelectronic properties of formamidinium tin triiodide thin films, *Adv. Mater.*, 30(2018), No. 44, art. No. 1804506.

[13] T.H. Wu, X. Liu, X.H. Luo, *et al*., Lead-free tin perovskite solar cells, *Joule*, 5(2021), No. 4, p. 863.

[14] W.Y. Gao, P.Z. Li, J.B. Chen, C.X. Ran, and Z.X. Wu, Interface engineering in tin perovskite solar cells, *Adv. Mater. Interfaces*, 6(2019), No. 24, art. No. 1901322.

[15] M. Aldamasy, Z. Iqbal, G.X. Li, *et al*., Challenges in tin perovskite solar cells, *Phys. Chem. Chem. Phys.*, 23(2021), No. 41, p. 23413.

[16] X. Zhang, S.R. Wang, W.K. Zhu, Z.Y. Cao, A.L. Wang, and F. Hao, The voltage loss in tin halide perovskite solar cells: Origins and perspectives, *Adv. Funct. Mater.*, 32(2022), No. 8, art. No. 2108832.

[17] B. Chen, S.R. Wang, X. Zhang, W.K. Zhu, Z.Y. Cao, and F. Hao, Reducing the interfacial voltage loss in tin halides perovskite solar cells, *Chem. Eng. J.*, 445(2022), art. No. 136769.

[18] W.S. Yang, J.H. Noh, N.J. Jeon, *et al*., High-performance photovoltaic perovskite layers fabricated through intramolecular exchange, *Science*, 348(2015), No. 6240, p. 1234.

[19] K. Nishimura, M.A. Kamarudin, D. Hirotani, *et al*., Lead-free tin-halide perovskite solar cells with 13% efficiency, *Nano Energy*, 74(2020), art. No. 104858.

[20] M. Konstantakou and T. Stergiopoulos, A critical review on tin halide perovskite solar cells, *J. Mater. Chem. A*, 5(2017), No. 23, p. 11518.

[21] W.F. Yang, F. Igbari, Y.H. Lou, Z.K. Wang, and L.S. Liao, Tin halide perovskites: Progress and challenges, *Adv. Energy Mater.*, 10(2020), No. 13, art. No. 1902584.

[22] Z.H. Zhang, Z.C. Li, L.Y. Meng, S.Y. Lien, and P. Gao, Perovskite-based tandem solar cells: Get the most out of the sun, *Adv. Funct. Mater.*, 30(2020), No. 38, art. No. 2001904.

[23] X. Liu, T.H. Wu, X.H. Luo, *et al*., Lead-free perovskite solar

1972

Int. J. Miner. Metall. Mater., Vol. 30, No. 10, Oct. 2023

cells with over 10% efficiency and size 1 cm^2 enabled by solvent-crystallization regulation in a two-step deposition method, *ACS Energy Lett.*, 7(2022), No. 1, p. 425.

[24] Z. Zhang, M.A. Kamarudin, A.K. Baranwal, *et al.*, Indent-free vapor-assisted surface passivation strategy toward tin halide perovskite solar cells, *ACS Appl. Mater. Interfaces*, 14(2022), No. 31, p. 36200.

[25] A. Al-Ashouri, E. Köhnen, B. Li, *et al.*, Monolithic perovskite/silicon tandem solar cell with >29% efficiency by enhanced hole extraction, *Science*, 370(2020), No. 6522, p. 1300.

[26] X. Liu, T.H. Wu, C.Y. Zhang, Y.Q. Zhang, H. Segawa, and L.Y. Han, Interface energy-level management toward efficient tin perovskite solar cells with hole-transport-layer-free structure, *Adv. Funct. Mater.*, 31(2021), No. 50, art. No. 2106560.

[27] W. Bumrungsan, K. Hongsith, V. Yarangsi, *et al.*, Efficiency enhancement of Cs$_{0.1}$(CH$_3$NH$_3$)$_{0.9}$PbI$_3$ perovskite solar cell by surface passivation using iso-butyl ammonium iodide, *Int. J. Miner. Metall. Mater.*, 29(2022), No. 11, p. 1963.

[28] Y.T. Xu, K.J. Jiang, P.C. Wang, *et al.*, Highly oriented quasi-2D layered tin halide perovskites with 2-thiopheneethylammonium iodide for efficient and stable tin perovskite solar cells, *New J. Chem.*, 46(2022), No. 5, p. 2259.

[29] Z.S. Dai, T. Lv, J. Barbaud, *et al.*, Stable tin perovskite solar cells developed via additive engineering, *Sci. China Mater.*, 64(2021), No. 11, p. 2645.

[30] X. Liu, Y.B. Wang, T.H. Wu, *et al.*, Efficient and stable tin perovskite solar cells enabled by amorphous-polycrystalline structure, *Nat. Commun.*, 11(2020), No. 1, art. No. 2678.

[31] M.M. Zhang, Z.G. Zhang, H.H. Cao, *et al.*, Recent progress in inorganic tin perovskite solar cells, *Mater. Today Energy*, 23(2022), art. No. 100891.

[32] G.X. Li, Z.H. Su, M. Li, *et al.*, Ionic liquid stabilizing high-efficiency tin halide perovskite solar cells, *Adv. Energy Mater.*, 11(2021), No. 32, art. No. 2101539.

[33] X. Liu, T.H. Wu, J.Y. Chen, *et al.*, Templated growth of FASnI$_3$ crystals for efficient tin perovskite solar cells, *Energy Environ. Sci.*, 13(2020), No. 9, p. 2896.

[34] B.B. Yu, Z.H. Chen, Y.D. Zhu, *et al.*, Heterogeneous 2D/3D tin-halides perovskite solar cells with certified conversion efficiency breaking 14%, *Adv. Mater.*, 33(2021), No. 36, art. No. 2102055.

[35] H.S. Li, X.Y. Jiang, Q. Wei, *et al.*, Low-dimensional inorganic tin perovskite solar cells prepared by templated growth, *Angew. Chem. Int. Ed.*, 60(2021), No. 30, p. 16330.

[36] M.A. Kamarudin, S.R. Sahamir, K. Nishimura, *et al.*, Suppression of defect and trap density through dimethylammonium-substituted tin perovskite solar cells, *ACS Mater. Lett.*, 4(2022), No. 9, p. 1855.

[37] F.D. Gu, C.B. Wang, Z.R. Zhao, *et al.*, Tin(II) acetylacetonate as a new type of tin compensator additive for tin-based perovskite solar cells, *ACS Appl. Mater. Interfaces*, 13(2021), No. 37, p. 44157.

[38] Z. Zhang, M.A. Kamarudin, A.K. Baranwal, *et al.*, Sequential passivation for lead-free tin perovskite solar cells with high effi-

ciency, *Angew. Chem. Int. Ed.*, 61(2022), No. 42, art. No. 202210101.

[39] S.R. Wang, L. Yan, W.K. Zhu, *et al.*, Suppressing the formation of tin vacancy yields efficient lead-free perovskite solar cells, *Nano Energy*, 99(2022), art. No. 107416.

[40] H.J. Yan, B.W. Wang, X.F. Yan, *et al.*, Efficient passivation of surface defects by lewis base in lead-free tin-based perovskite solar cells, *Mater. Today Energy*, 27(2022), art. No. 101038.

[41] Z. Zhang, L. Wang, A.K. Baranwal, *et al.*, Enhanced efficiency and stability in Sn-based perovskite solar cells by trimethylsilyl halide surface passivation, *J. Energy Chem.*, 71(2022), p. 604.

[42] E. Jokar, C.H. Chien, A. Fathi, M. Rameez, Y.H. Chang, and E.W.G. Diau, Slow surface passivation and crystal relaxation with additives to improve device performance and durability for tin-based perovskite solar cells, *Energy Environ. Sci.*, 11(2018), No. 9, p. 2353.

[43] C. Liu, J. Tu, X.T. Hu, *et al.*, Enhanced hole transportation for inverted tin-based perovskite solar cells with high performance and stability, *Adv. Funct. Mater.*, 29(2019), No. 18, art. No. 1808059.

[44] E. Jokar, H.S. Chuang, C.H. Kuan, *et al.*, Slow passivation and inverted hysteresis for hybrid tin perovskite solar cells attaining 13.5% via sequential deposition, *J. Phys. Chem. Lett.*, 12(2021), No. 41, p. 10106.

[45] B.H. Chang, B. Li., Z.X. Wang, *et al.*, Efficient bulk defect suppression strategy in FASnI$_3$ perovskite for photovoltaic performance enhancement, *Adv. Funct. Mater.*, 32(2022), No. 12, art. No. 2107710.

[46] P.J. Zhao, B.J. Kim, and H.S. Jung, Passivation in perovskite solar cells: A review, *Mater. Today Energy*, 7(2018), p. 267.

[47] Q.D. Tai, X.Y. Guo, G.Q. Tang, *et al.*, Antioxidant grain passivation for air-stable tin-based perovskite solar cells, *Angew. Chem. Int. Ed.*, 58(2019), No. 3, p. 806.

[48] J.Y. Kim, J.W. Lee, H.S. Jung, H. Shin, and N.G. Park, High-efficiency perovskite solar cells, *Chem. Rev.*, 120(2020), No. 15, p. 7867.

[49] Y. Zhang, Y. Li, L. Zhang, *et al.*, Propylammonium chloride additive for efficient and stable FAPbI$_3$ perovskite solar cells, *Adv. Energy Mater.*, 11(2021), No. 47, art. No. 2102538.

[50] D.S. Yao, C.M. Zhang, S.L. Zhang, *et al.*, 2D–3D mixed organic–inorganic perovskite layers for solar cells with enhanced efficiency and stability induced by *n*-propylammonium iodide additives, *ACS Appl. Mater. Interfaces*, 11(2019), No. 33, p. 29753.

[51] D.D. Wu, P.C. Jia, W.T. Bi, *et al.*, Enhanced performance of tin halide perovskite solar cells by addition of hydrazine monohydrobromide, *Org. Electron.*, 82(2020), art. No. 105728.

[52] P.C. Jia, L. Qin, D. Zhao, *et al.*, The trapped charges at grain boundaries in perovskite solar cells, *Adv. Funct. Mater.*, 31(2021), No. 49, art. No. 2107125.

[53] C.X. Ran, W.Y. Gao, J.R. Li, *et al.*, Conjugated organic cations enable efficient self-healing FASnI$_3$ solar cells, *Joule*, 3(2019), No. 12, p. 3072.